

Generative Residual Diffusion Modeling for Km-scale Atmospheric Downscaling

Morteza Mardani^{1,*a}, Noah Brenowitz^{1,*}, Yair Cohen^{1,*}, Jaideep Pathak¹, Chieh-Yu Chen¹, Cheng-Chin Liu², Arash Vahdat¹, Karthik Kashinath¹, Jan Kautz¹, and Mike Pritchard¹

¹*NVIDIA, Santa Clara, CA. 95050, USA*

²*Central Weather Administration, 64, Gongyuan Road, Taipei 100006, Taiwan*

^{*}*These authors contributed equally*

^a*Corresponding author: mmardani@nvidia.com*

October 2, 2023

Abstract

The state of the art for physical hazard prediction from weather and climate requires expensive km-scale numerical simulations driven by coarser resolution global inputs. Here, a km-scale downscaling diffusion model is presented as a cost effective alternative. The model is trained from a regional high-resolution weather model over Taiwan, and conditioned on ERA5 reanalysis data. To address the downscaling uncertainties, large resolution ratios (25km to 2km), different physics involved at different scales and predict channels that are not in the input data, we employ a two-step approach (*ResDiff*) where a (UNet) regression predicts the mean in the first step and a diffusion model predicts the residual in the second step. *ResDiff* exhibits encouraging skill in bulk RMSE and CRPS scores. The predicted spectra and distributions from ResDiff faithfully recover important power law relationships regulating damaging wind and rain extremes. Case studies of coherent weather phenomena reveal appropriate multivariate relationships reminiscent of learnt physics. This includes the sharp wind and temperature variations that co-locate with intense rainfall in a cold front, and the extreme winds and rainfall bands that surround the eyewall of typhoons. Some evidence of simultaneous bias correction is found. A first attempt at downscaling directly from an operational global forecast model successfully retains many of these benefits. The implication is that a new era of fully end-to-end, global-to-regional machine learning weather prediction is likely near at hand.

1 Introduction

Coarse-resolution (25-km) global weather prediction is undergoing a machine learning renaissance thanks to autoregressive machine learning models that have successfully exploited readily available reanalysis data with global coverage at these spatial scales [5, 32, 9, 6, 24, 10].

However, users of weather data generally need higher-resolution predictions. Kilometer-scale atmospheric models better capture extremes, such as damaging winds and rainfall, as well as important local effects of mountains, agriculture and urban land use, which regulate the local weather and its impact at the scales of physical infrastructure [16].

It is thus natural to wonder if one can apply these ML models at km-scale resolutions. If tried globally, this poses a significant challenge. The linear increase in the resolution of training data typically results in a superlinear increase in the training cost of autoregressive ML surrogate models. Moreover, global km-scale simulations are in their infancy [49, 21] with data that tends to cover short periods of time, do not assimilate km-scale observations, and are not as heavily tuned so may have worse systematic biases than coarse-resolution or established regional simulations. Such massive datasets are also difficult to transfer between data centers and are frequently not produced on machines attached to significant accelerated computing resources like GPUs.

In contrast, for regional simulation, scaling ML to km-scales is attractive. High quality training data is abundant as many national weather agencies couple km-scale numerical weather models in a limited domain to coarser resolution global models [41]. Since these predictions are augmented by data assimilation from ground-based precipitation radar and other sensors, good estimates of regional km-scale atmospheric states are possible – a process called dynamical downscaling.

However, dynamical downscaling is a computationally expensive approach that limits the number of ensemble members that can be used to quantify uncertainties [31]. An alternative approach is to learn a computationally inexpensive statistical downscaling from these dynamical downscaling models and observations, thus allowing larger ensembles and better uncertainty quantification [53]. Statistical downscaling is considered less reliable, especially for extreme events. In this context, ML downscaling enters as an advanced (non linear) form of statistical downscaling that exhibits improved predictions.

Various ML methods have been previously used for atmospheric downscaling [44, 13, 50, 31, 52]. Convolutional Neural Networks (CNNs), which reduce input vector and identify crucial features, have shown promise in globally downscaling climate (100km) data to weather scales (25km) [29, 40, 2, 38]. However, their deterministic nature requires some custom approaches to produce a probability (i.e., ensemble inference [40] or predicting parameters of an assumed distribution [2]).

The stochastic nature of atmospheric physics at km-scale [45] makes the downscaling inherently probabilistic. It is thus natural to apply generative models for downscaling at these scales. Generative Adversarial Networks (GANs) have been used in downscaling and forecasting precipitation at km-scale in various regions [26, 36, 17, 39, 15, 52], see the latter for a good review of these works. Training GANs however poses several challenges including mode collapse, training instabilities, and difficulties in capturing long tails of distributions [54, 23, 42].

Diffusion models have been recently introduced as a viable alternative to GANs due to their sample diversity and training stability [20, 11]. They are based on principles of stochastic differential equations (SDE) and use a tandem of noising and denoising processes to learn the data distribution. The former process gradually adds noise until the data turns to noise. The latter process then gradually removes noise to recover the data. They have demonstrated a remarkable ability to generate fine-scale details of samples for both unconditional and conditional image generation tasks. Diffusion models proved successful for downscaling of a single variable to km-scale. [1] produced the full rain density in the UK from vorticity as an input, thus showing channel synthesis abilities - beyond super-resolution, predicting variables that are not in the input data. [18] used a diffusion model for downscaling solar irradiance in Hawaii with a 1 day lead time, thus demonstrating the ability of this model to account for lead time biases. Moreover, diffusion models have been used for probabilistic weather forecasting and nowcasting [25, 27].

The success in ML downscaling of a single variable from global numerical weather models to km-scale motivates us to an ambitious goal: Can we downscale several variables in concert – including variables that are not in the input? If so, this paves the way towards end-to-end ML downscaling systems that predict regional high-resolution weather as a postprocessing of 25-km scale ML predictions. We will show a proof-of-concept of the feasibility of such systems.

To that end, we develop a diffusion model that performs multi-variable downscaling with channel synthesis and test its downscaling abilities from a numerical global weather model at lead times of up to 3 days. We train the model on high resolution data for the region of Taiwan. This, target, data is produced using a radar-assimilating configuration of the Weather Research and Forecasting (WRF) model [34] and were provided to us by the Central Weather Administration of Taiwan (CWA).

In the case of km-scale downscaling, direct application of diffusion models for learning the distribution of high-resolution states is challenging because coarse-resolution data produced from a global model (the input) and high-resolution data produced from a regional km-scale model (the target) approximate the underlying governing equations in different ways. This results in a significant distribution shift between the input and target data. Such distribution shift impedes conditioning of diffusion models, and thus necessitates large noise levels for the diffusion noising process, and consequently many steps for the backward process to remove noise, ultimately resulting in poor generation fidelity.

To address these challenges, we demonstrate a two-stage approach for downscaling (see e.g. [36]). In the first stage, a UNet-regression predicts the conditional mean of the high-resolution state based on the coarse-resolution input. In the second stage, a denoising diffusion model is trained on the residuals (difference between the truth and the regression, both at high-resolution). Since the residuals have significantly smaller

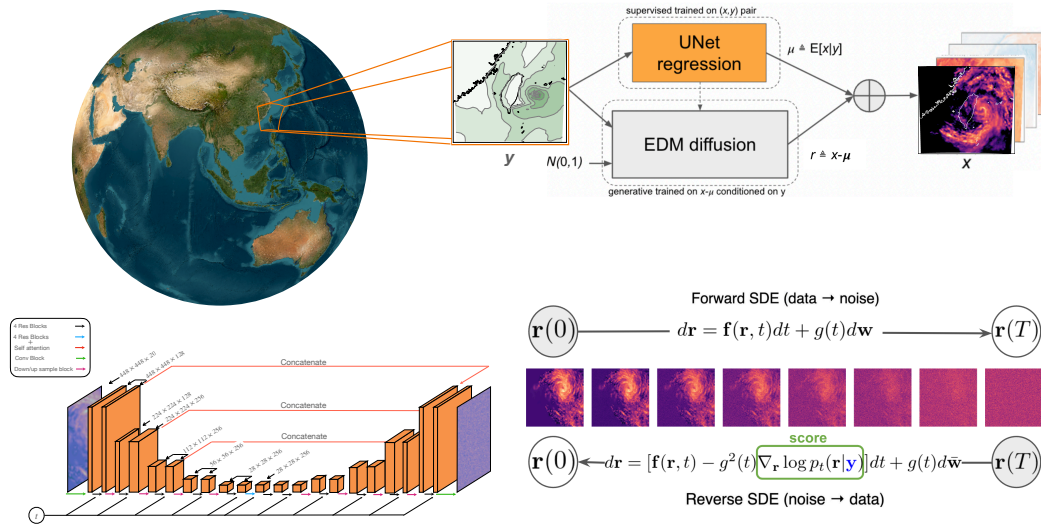


Figure 1: The workflow for training and sampling ResDiff for generative downscaling. Top: a coarse-resolution global forecast at 25km scale is used to predict the mean μ first, and is then added with the residual predicted using EDM denoising diffusion \mathbf{r} to generate the high-resolution 2km-scale regional forecast. Bottom right: diffusion model is conditioned with the coarse-resolution input to generate the residual \mathbf{r} after a few denoising steps. Bottom left: the score function for diffusion is learned based on the UNet architecture.

values and are nearly centered compared with the high-resolution forecasts, the denoising diffusion process is easier to learn. This approach greatly facilitates training and sampling of diffusion models, enabling more accurate representation of regional details. In this work, for the diffusion stage, we adopt Elucidated Diffusion Models (EDM) [22], for their high generation quality in unconditional generation tasks and their adaptive tuning inspired by SDEs and physics.

In the next section we outline details of the model. The key contributions of this paper are:

1. A novel physics-inspired two-step approach (ResDiff) to learn mappings between low- and high-resolution weather data with high fidelity, including for extreme weather events that occur infrequently in the training data, like typhoons.
2. ResDiff provides realistic measures of stochasticity and uncertainty, in terms of Continuous Rank Probability Score (CRPS) and by comparing spectra and distributions.
3. ResDiff learns the physics of coherent weather phenomena remarkably well, as measured by the corrections of the discontinuity across a frontal systems and of the axi-symmetric spatial structure and intensity of typhoon winds.
4. ResDiff is sample-efficient, learning effectively from just 4 years of data, which we hypothesize is due to the two-step approach to learning the mean and residuals of complex distribution shifts between the low- and high-resolution data.
5. ResDiff is at least 60 times faster and 100 times more energy efficient than WRF used by CWA, providing an attractive alternative (or complementary method) for dynamical downscaling techniques.

2 Generative downscaling: residual diffusion models

Consider a specific region on Earth, mapped onto a two-dimensional grid. Within this spatial representation, we can extract a low-resolution meteorological forecast using a global weather forecasting model such as FourCastNet [32] or the Global Forecast System (GFS) [30]. This low-resolution forecast, e.g., of 25km resolution, is denoted as $\mathbf{y} \in \mathbb{R}^{c_{\text{in}} \times m \times m}$. In this context, c_{in} represents various global forecast variables, which include, e.g., surface wind and temperature.

The high-resolution data are denoted as $\mathbf{x} \in \mathbb{R}^{c_{\text{out}} \times n \times n}$. Note that \mathbf{x} and \mathbf{y} are solutions to different sets of PDEs, with significantly different resolutions ($n \gg m$), each influenced by distinct scale-dependent physics, e.g., radiation and cloud processes. This leads to a significant distribution shift between the low- and high-resolution data. Downscaling to km-scale comes with large uncertainties because the dynamics of the atmosphere at km-scale is highly stochastic and exhibits large spatial and temporal variability. Thus, the goal of probabilistic downscaling is to mimic the probability density $p(\mathbf{x}|\mathbf{y})$.

To learn the conditional density $p(\mathbf{x}|\mathbf{y})$ for generation, we employ diffusion models due to their excellent distribution mode coverage and stable training [11]. Diffusion models solve stochastic differential equations (SDEs) through the concept of score matching [20, 47, 22, 46, 4]. This requires a forward process and a backward process that work in tandem. In the forward process, noise is gradually added to the data until the signal becomes indistinguishable from noise. This step allows the diffusion model to explore and capture the intricate patterns and dependencies present in the data. By incrementally introducing noise, the model gains a deeper understanding of the underlying distribution. The backward process then involves denoising the samples using a dedicated neural network to eliminate the noise. Through this sequential denoising process, the model iteratively refines the samples, bringing them closer to the true data distribution. The denoising neural network plays a critical role in this convergence, providing the necessary guidance to steer the samples towards accurate representations of the original data.

Naively applying conditional diffusion models to learn $p(\mathbf{x}|\mathbf{y})$ was unsuccessful for downscaling because of the aforementioned large distribution shift and the large uncertainty of variables such as radar reflectivity at these scales. As a result, the diffusion forward process requires substantial noise levels to ensure that the signal ultimately transforms into pure noise. Consequently, the backward process, which gradually removes noise and generates the clean signal, demands a large number of steps. This impedes learning and leads to poor sample fidelity.

To sidestep these challenges, we propose to decompose the generation into two stages: The first stage predicts the conditional mean using (UNet) regression, and the second stage learns a generative diffusion model on the residuals, inspired by the common practice in fluid dynamics to decompose a flow into its mean and perturbation [33]. Following this ansatz, we decompose the fine-resolution forecast as

$$\mathbf{x} = \underbrace{\mathbb{E}[\mathbf{x}|\mathbf{y}]}_{:=\boldsymbol{\mu}(\text{regression})} + \underbrace{(\mathbf{x} - \mathbb{E}[\mathbf{x}|\mathbf{y}])}_{:=\mathbf{r}(\text{generation})} \quad (1)$$

In this decomposition the regression mean ($\boldsymbol{\mu}$) matches the first-moment of the data distribution. As a result the residual (\mathbf{r}) becomes approximately zero mean that leads to a significantly smaller variance for the residual distribution, namely $\text{var}(\mathbf{r}) \ll \text{var}(\mathbf{x})$, when the forecast has large variations (see section 7.3 for the proof). Hence, learning the distribution $p(\mathbf{r}|\mathbf{y})$ becomes easier for the generative diffusion model. The details are described in section 5 and the outline is depicted in Fig. 1.

In the next section we examine the key results of using this model for atmospheric downscaling.

3 Results

We compare predictions from ResDiff with the input data (ERA5, [19]), several baseline models and the target data (WRF). We validate the performance by examining deterministic and probabilistic skill scores, distributions and power spectra, as well as case studies showcasing representative forecasts of various coherent atmospheric phenomena such as typhoons and atmospheric fronts.

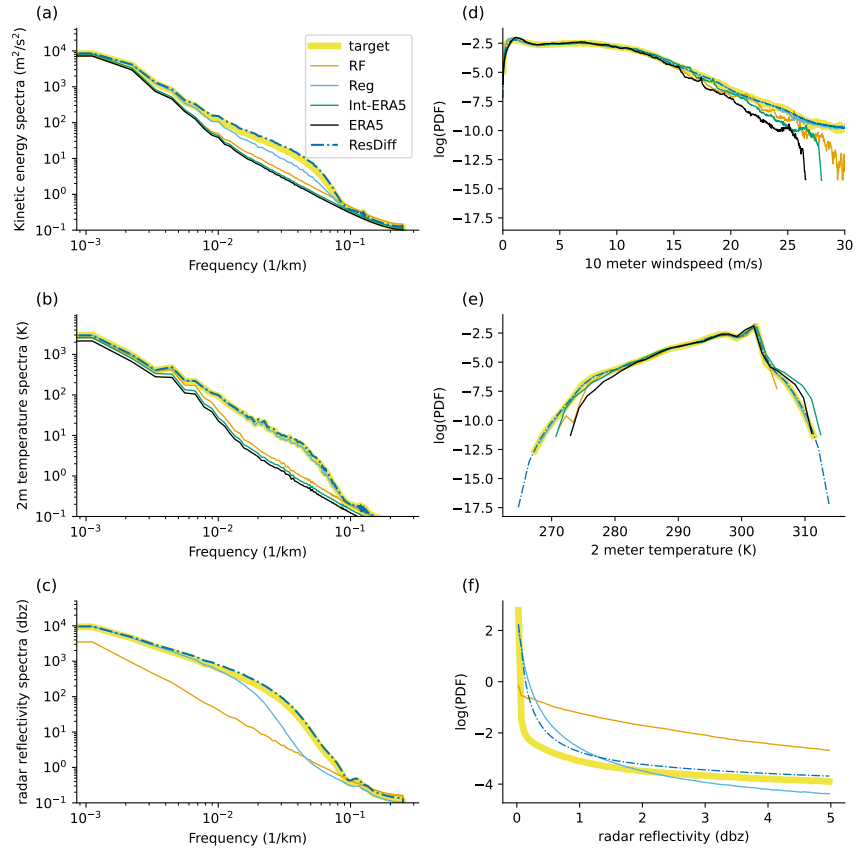


Figure 2: Power spectra and distributions for the interpolated ERA5 input, ResDiff, RF, Reg, and WRF. These results reflect reductions over space, time and for *ResDiff* ensemble dimensions. Left: Power spectra for kinetic energy (top), 2 meter temperature (middle) and radar reflectivity (bottom). Right: distributions of windspeed, (top), 2 meter temperature (middle) and radar reflectivity (bottom). Radar reflectivity is not included in the ERA5 dataset. We show the log-PDF to highlight the differences at the tails of the distributions.

Method	Metric	u10m	Radar	v10m	t2m
ResDiff	CRPS	0.29	0.53	0.31	0.14
ResDiff	MAE	0.40	0.74	0.43	0.19
UNet-regression	MAE	0.45	0.77	0.50	0.24
Random forest regression	MAE	1.15	3.58	1.28	0.81
ERA5 bilinear interpolation	MAE	1.18	-	1.28	0.97

Table 1: Skill scores evaluated over 204 time samples with 192 ensemble members. The table compares ResDiff, UNet-regression, random forest, and interpolated ERA5 predictions in terms of MAE of the ensemble mean and CRPS for different atmospheric variables. For deterministic predictions, MAE and CRPS are equivalent.

3.1 Skill

Table 1 shows the skill scores for ResDiff and several baseline models for 204 samples taken randomly from the out-of-sample year (2021). The baseline models are random forest (RF), a UNet-regression (Reg) and the bilinearly interpolated ERA5 inputs. Since all of these are deterministic models, we only show MAE scores for them, recalling that MAE equals CRPS for a deterministic model. For ResDiff MAE represents the error of the sample mean. RF is trained by selecting spatial samples from 200 randomly selected times within the training period. A separate RF is fit with `scikit-learn` for each of the 4 output channels with 100 trees and the default hyperparameters. While crude, this RF provides a simple (and easily tuned) baseline for the performance of Reg.

ResDiff has the highest deterministic skill (MAE) followed by the UNet regression, the RF and the interpolation of ERA5. The difference between MAE of ResDiff and that of the UNet reflects the correction of the sample mean by the diffusion model. The consistent improvement in MAE for all the target variables between the UNet and ResDiff suggests that the generative ResDiff model (step 2) can correct some of the remaining biases after the UNet-regression stage (step 1).

Finally, we compare the speed of ResDiff against the operational WRF run by CWA. The CWA-WRF is run on Fujitsu FX-100 system, where each node is equipped with 32 SPARC64 Xifx CPU cores. One hour of a deterministic CWA-WRF forecast (excluding data assimilation) is run on 928 CPU cores (across 29 nodes with a maximum system memory of 6.9GB per node) and takes about 20min. ResDiff inference is however run on a single A100 GPU with 40GB RAM, which takes 24 sec per downscaling sample. Per frame, ResDiff is about 60 times faster than CWA-WRF, and on these hardware systems, it is about 100 times more energy efficient as well. We note that our current implementation of ResDiff is far from optimized and does not utilize GPU parallelization and batching for generating many samples independently. We believe that GPU parallelization, batched inference, as well as fp16 precision will likely lead to even more significant speed-up.

3.2 Spectra and distributions

To produce spectra and distributions we perform a reduction of the predictions from the various models across space and time, and for ResDiff additionally across the ensemble dimension. The left column of Fig. 2 shows the ability of ResDiff to correct the power spectra of kinetic energy (KE), 2-meter temperature and radar reflectivity compared with the various models examined in Table 1 and from ERA5 (where radar reflectivity is absent). For all variables the ResDiff predictions match the target spectra closely. We observe that the performance of UNet-regression is comparable to ResDiff in predicting 2-meter temperature, but slightly less effective in predicting kinetic energy. This implies that stochastic factors are not significant for 2-meter temperature predictions, while they have some, but limited, impact on kinetic energy predictions. However, for radar reflectivity the power spectra of the UNet-regression is significantly worse than ResDiff, suggesting that stochasticity is especially important for this field (see also [52]). Small-scale temperature is mostly driven by horizontal variations in topography in this data which can be learned from the grid embeddings, which are a static input. Radar reflectivity comes from precipitation, which is linked to intrinsically stochastic physics; ResDiff produces a skillful match to the radar spectrum.

Good skill is also found when looking at the probability distributions from these models (right panels of

Fig. 2), for which we switch focus from kinetic energy to wind speed, which is more relevant to physical hazard evaluation in risk assessment. ResDiff is able to match the target distribution, including the heavy-tailed structure which is significantly improved from the prediction based on the UNet alone.

For windspeed, the UNet and the baseline models underestimate the probability of winds faster than 20 m/s. For 2-meter temperatures, the baseline models overestimate the probability of warm extremes and underestimate the probability of cold extremes. Radar reflectivity proves to be the most challenging distribution to reproduce. ResDiff outperforms the other models in reproducing the reflectivity. Although it overestimates the occurrence of reflectivity at lower values (i.e. weakly precipitating systems), the match of slopes at high values attests that the power-law relationship regulating the heavy-tail structure of rain extremes is captured well.

3.3 Case studies: downscaling coherent structures

Operational meteorologists value case study analysis, since aggregate skill scores and spectra can be more easily gamed. We thus turn our attention to specific weather regimes. Fig. 3 illustrates the variability of the generated radar reflectivity field at four distinct times. When analyzing 200 samples, the standard deviation of radar reflectivity (second column from the left) is roughly 20% of the magnitude of the mean (left column), with the majority of the variance located in and around existing precipitation regions. Such a pattern is anticipated given that the timing and location of precipitation can vary markedly even within a fixed large-scale configuration since convective physics are inherently stochastic.

The ResDiff prediction for an individual sample (number 200, third column from the left) reveals a fine-scale structure akin to the target data (right column). The similarity between panels (a) and (d) highlights the role of the mean prediction in forming large-scale coherent structures, such as typhoon Chanthu (2021), top row, and frontal systems, bottom row. Specifically the typhoon rainbands (spiral bands of clouds that emanate from the typhoon center) are coherent enough to be captured by the mean, but with large variance and smooth structure. The fine-scale structure reflecting the stochastic physics is captured well by the diffusion model, refining the smooth fields of the mean prediction as seen in the third column of Fig. 3.

3.3.1 Frontal system case study

Frontal systems are an example of organized atmospheric systems. A cold front is a sharp change in temperature and winds associated with a mature cyclonic storm. Fronts produce rainfall since as the front moves eastward, the cold air pushes the warm air to its east upward. This upward motion leads to cooling, condensation and ultimately rainfall. That is, these physics should manifest as multi-variate relationships with linked fine scale structures of two wind vector components and temperature that should co-locate with radar reflectivity.

Fig. 4 shows an example of ResDiff downscaling a cold front. The position of the front is clearly visible in the southeast portion of the domain, where a strong horizontal surface temperature gradient (top) co-locates with strong across-front wind convergence (middle). The along-front components of the wind vector also change abruptly (middle row), which is consistent with the change in temperature. The super resolved gradients in the temperature and winds are encouragingly sharper than the input. The intense rainfall associated with this convergence line can be seen in the radar reflectivity ground truth for the same calendar date (which are shown in bottom row of Fig. 3 above). The generated radar reflectivity is appropriately concentrated near the frontal boundary. Both the location of the front, and the magnitude of the horizontal wind and temperature gradients (sharpening of the front) associated with it, are captured well by ResDiff although some mispositioning of the exact front location is inevitable. These are reassuring signs of learnt physics during the generation task.

3.3.2 Tropical Cyclone case study

Downscaling typhoons (i.e. tropical cyclones) is especially complicated. The average radius of maximum winds of a tropical cyclone is less than 100km, and at 25km resolution of the input data tropical cyclones are only partially resolved, resulting in cyclonic structures that are too wide and too weak compared with high resolution models or observations [7]. A useful downscaling model must simultaneously correct their size and intensity in addition to generating appropriate fine-scale structure.

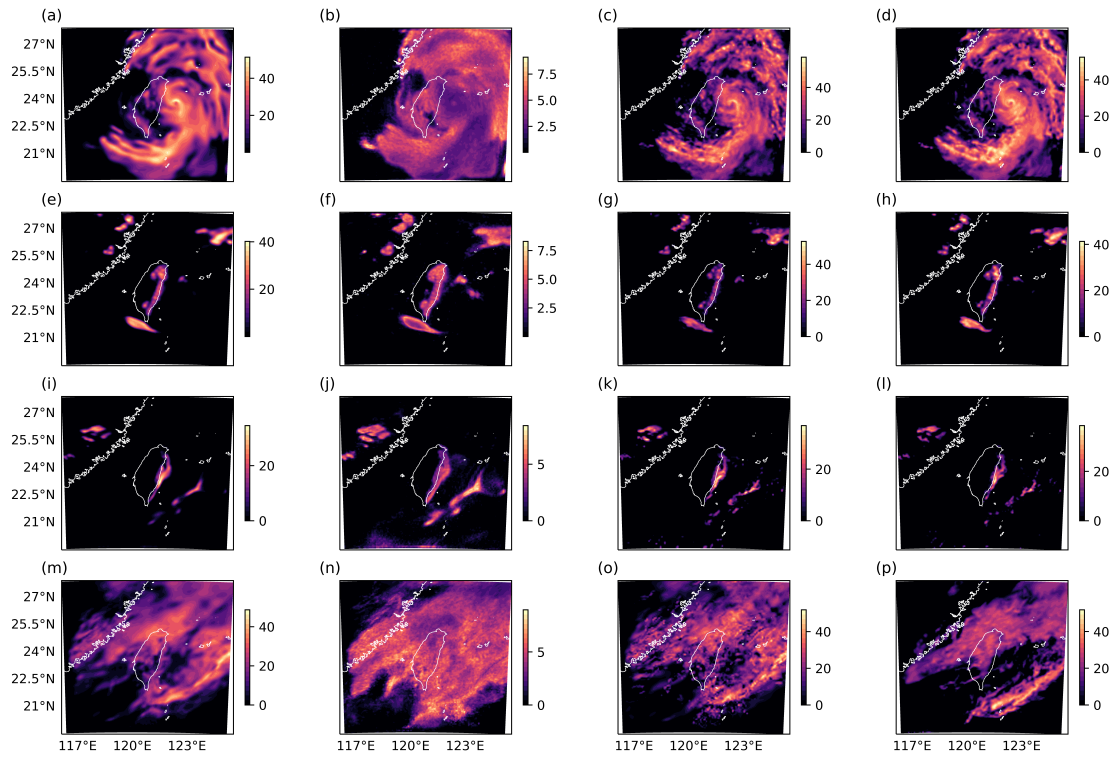


Figure 3: Demonstration of the stochastic prediction of radar reflectivity (in dBZ). Top to bottom: 2021-09-12 00:00, 2021-04-02 06:00, 2021-02-02 12:00 and 2022-02-13 20:00. Left to right: sample mean, sample standard deviation, sample number 200 and the target forecast.

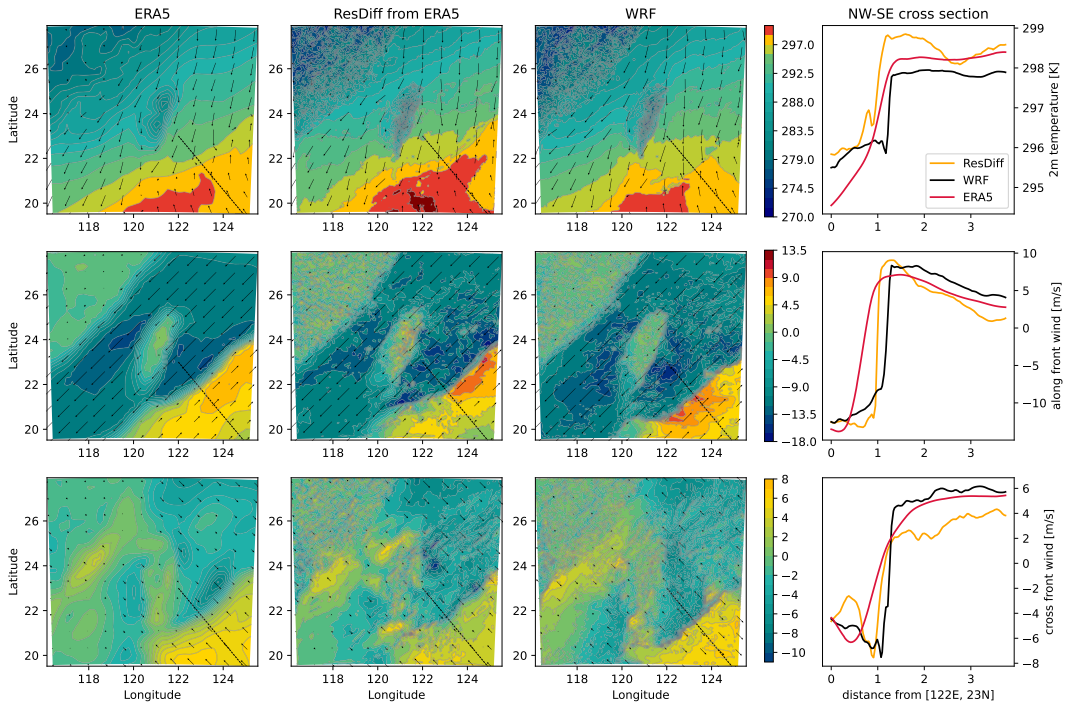


Figure 4: Examining the downscaling of a cold front on Feb 2, 2022 at 20 UTC. Left to right: prediction of ERA5, ResDiff and Target for different fields, followed by their averaged cross section from 20 lines parallel to the thin dashed line in the contour figures. Top to bottom: 2 meter temperature (arrows are true wind vectors), along front wind (arrows are along front wind component) and across front wind (arrows are across front wind component).

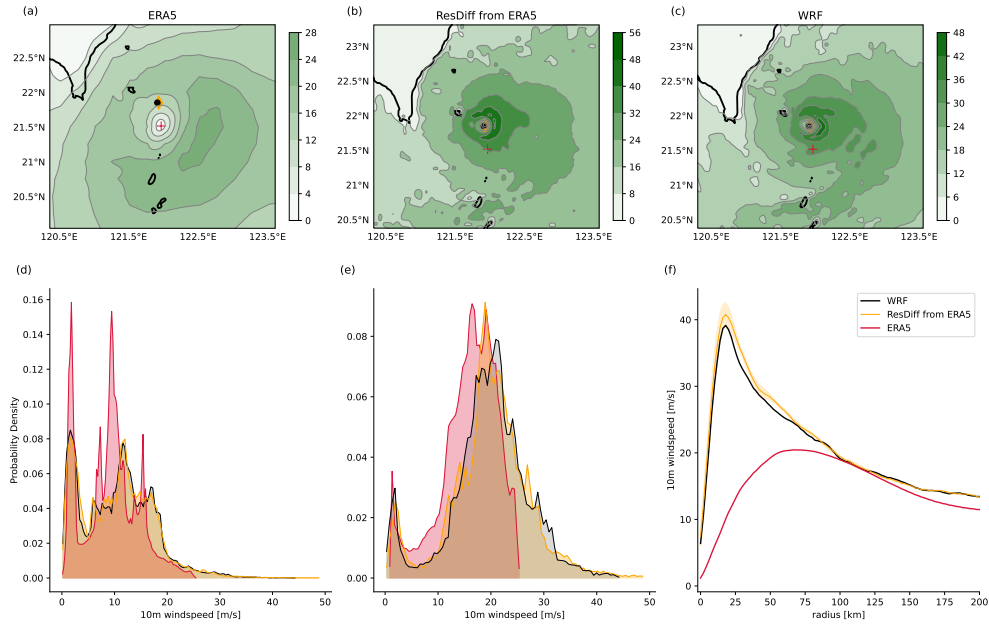


Figure 5: A comparison of the 10m windspeed (m/s) maps, distributions and the axisymmetric cross section from typhoon Chanthu (2021) on 2021/09/11:12:00:00UTC. Panels (a),(b),(c) show the 10m windspeed from ERA5, ResDiff downscaling of ERA5 and the target (WRF), respectively. The ResDiff panels show the first ensemble member. The solid black contour indicates the Taiwan coastline. Storm center of the ERA5, ResDiff and WRF are shown in red ‘+’, orange diamond, and the black dot, respectively. Panels (d) and (e) show the distribution shift (normalized PDFs) for the entire CWA domain and for the typhoon selected region in the top panels. Panel (f) shows the axisymmetric structure of the typhoon about its center. For the ResDiff curves, line is the ensemble mean and the shading shows one standard deviation around the mean.

We find that ResDiff is able to correct the structure of tropical cyclones accurately. Fig. 5(a)-(f) shows the structure of typhoon Chanthu (2021), the only typhoon that entered the domain in the out-of-sample year, on September 12 at 00:00:00 UTC. Compared to the target data (panel c) the poorly resolved typhoon in the ERA5 (panel a) is too wide and does not include a closed contour annulus of winds above 16 m/s surrounding an overly quiescent eye-wall. ResDiff downscaling (panel b) is able to recover much of the spatial structure of the windspeed compared with the target. The improvement in the location of the typhoon’s center could be a combination of improved prediction and the increase in resolution. The skill of the ResDiff downscaling compared to interpolating ERA5 can be more clearly quantified by calculating the mean axisymmetric structure of the storms as a function of radius from eye-wall center (panel f). Notably, with downscaling the radius of maximum winds decreases from 75km to about 25km while the windspeed increases from 20 m/s to 50 m/s – both favorable improvements.

Probabilities of damaging typhoon winds shown in in panels (d) and (e) in Fig. 5 are significantly improved. In ERA5 (red), occurrence of weak wind speeds is over-estimated and the damaging extreme hurricane winds (above 25m/s) are missing. ResDiff better predicts the chances of the strong winds most likely to impact society and infrastructure. Further analysis (see supplementary material) expands beyond this case study to examine generated wind statistics for several hundred typhoons that crossed the domain during 1980 to 2020. Although no target data is available, when comparing the maximum windspeed and radius of maximum windspeed from ResDiff predictions to a reference from the Japan Meteorological Agency best track dataset [3] ResDiff is found to correct at least 75% of the error in intensity for windspeed below 50m/s but only 50% of the error for higher windspeeds.

3.4 Downscaling a forecast from a global model

An attractive use case for ResDiff is to replace dynamical downscaling for regional weather prediction, by instead directly postprocessing predictions from coarse resolution global forecast models. This is a challenging use case as it adds out of sample forecast bias to the input. We nonetheless attempt such "zero-shot" downscaling of a deterministic forecast from the GFS model for a two-day interval. We revisit Typhoon Chanthu (2021) as in the course of 24h such coherent structures facilitate a clear distinction between the trajectory error as a forecast lead time error, and the intensity error as a model resolution and physics related error. An expected enhancement in windspeed intensity is confirmed. At short lead time ResDiff is correcting the typhoon structure well. With increased lead time an error in the position of the typhoon is unavoidable in ResDiff and the coherent structure becomes increasingly degraded relative to the ground truth. This suggests that ResDiff could be used for downscaling from a global model at lead times of up to 48h. For longer lead times, fine-tuning ResDiff to anticipate the existence of global model forecast bias is a logical path.

4 Discussion

This study presents a diffusion based, generative, machine learning approach (ResDiff) for downscaling coarse-resolution (25-km) global weather state data (such as ERA5 or GFS) to higher resolution (2km) over a limited regional domain where high quality fine-scale state estimates exist. ResDiff consists of two steps: regression and generation. The regression step approximates the mean, while the generation step further corrects the mean but also generates the distribution, accounting for the fine-scale details stochastically. This approach is akin to the decomposition of physical variables into their mean and perturbations, common practice in fluid dynamics, e.g. [33].

Through extensive testing in the region of Taiwan, we evaluate the skill of the model for high-resolution regional downscaling. The model is shown to skillfully correct kinetic energy spectra, generate realistic probabilities of fine-scale weather extremes, and downscale coherent structures accurately, with minor caveats such as inaccuracies in the 2-meter temperature on the warm sector of a frontal system (4) and over-correction of typhoon sizes in some out-of-sample cases for which we do not have the target (WRF) data (see SI). The model's accuracy could be further improved with a larger training dataset that contains more diverse examples of such rare coherent structures.

The two step approach in ResDiff also offers the possibility to trade off between the fast inference of the mean using the UNet-regression, and the accurate and probabilistic inference of the ResDiff. This is particularly useful given that some variables – like the 2 meter temperature – are well predicted by the UNet-regression while others like radar reflectivity depend on the diffusion step for their skill (see figure 2). Moreover, it could be possible to apply the diffusion stage to a mean prediction obtained in a different way (e.g. a numerical model if available) to generate a plausible distribution from a single prediction.

This paper focused on generation quality, and not on optimal inference speed, for which gains could be easily anticipated. Our prototype of ResDiff is using a dozen iterations thanks to the initial regression stage. However, for future work, we will push to reduce the number of iterations to only a few by using distillation methods [43, 54, 55] and pursue other performance optimization techniques [28, 51].

Several potential extensions of the proposed method are worth considering:

1. **Downscaling Coarse-Resolution Medium-Range Forecasts:** To achieve this, it is essential to further quantify and incorporate lead time-dependent forecast errors into the training dataset, enabling a comprehensive evaluation of simultaneous bias correction and downscaling.
2. **Downscaling Different Geographic Locations:** The primary obstacle here is the scarcity of reliable kilometer-scale weather data. Additionally, addressing the computational scalability of ResDiff for regions significantly larger than Taiwan is crucial.
3. **Downscaling Future Climate Predictions:** This introduces further complexities related to conditioning probabilistic predictions on various future anthropogenic emissions scenarios and assessing whether the generated weather envelope appropriately reflects climate sensitivity, particularly concerning extreme events.

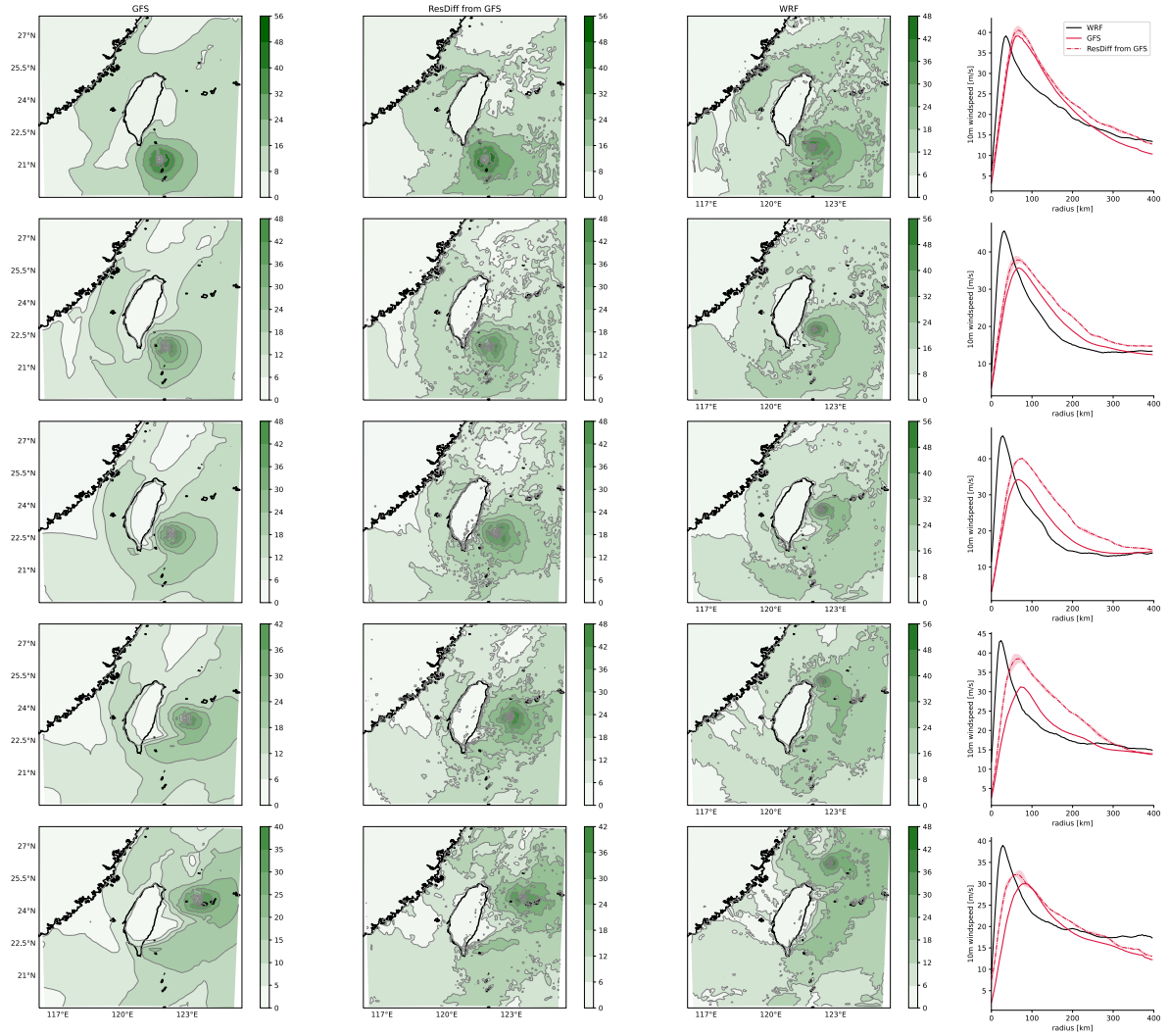


Figure 6: ResDiff downscaling from forecast. Comparison of the 10 meter windspeed forecast of typhoon Chanthu (2021) initialized 2021-09-10 00:00UTC. Left to right, first column: forecast from the GFS; second column: ResDiff downscaling of GFS, third column target and fourth column: axisymmetric profile of the typhoon in three models (shading for GFS+ResDiff shows one standard deviation). Top to bottom: results at 2021-09-11 12:00UTC, 2021-09-11 18:00UTC, 2021-09-12 00:00UTC, 2021-09-12 06:00UTC, 2021-09-12 12:00UTC and 2021-09-12 18:00UTC.

4. **Downscaling Outside the Training Region:** Transfer learning could become a viable strategy to extend results beyond the borders of existing km-scale data regions to geographically adjacent or dynamically self-similar regional weather regimes, allowing for more extensive usability.

These extensions have significant potential benefits such as accelerated regional forecasts, increased ensemble sizes, improved climate downscaling, and the provision of high-resolution regional forecasts in data-scarce regions, leveraging training data from adjacent areas.

5 Methods

This section elaborates on the proposed ResDiff methodology for probabilistic downscaling. It begins with a background on diffusion models to provide the machinery. It then delves into ResDiff and its associated components. We further detail our experimental setup including the CWA dataset, network architecture, and training protocols. At the end, we briefly discuss evaluation criteria.

5.1 Background on diffusion models

Consider the data distribution represented by $p_{\text{data}}(\mathbf{x})$. This distribution has an associated standard deviation, denoted by σ_{data} . The forward diffusion process seeks to adjust this distribution, yielding modified distributions denoted by $p_{\text{data}}(\mathbf{x}; \sigma)$. This transformation is achieved by incorporating i.i.d. Gaussian noise with a standard deviation of σ into the data. When σ surpasses σ_{data} by a considerable margin, the resulting distribution approximates pure Gaussian noise.

Conversely, the backward diffusion process operates by initially sampling noise, represented as \mathbf{x}_0 , from the distribution $\mathcal{N}(0, \sigma_{\text{max}}^2 \mathbf{I})$. The process then focuses on the denoising of this image into a series, \mathbf{x}_i , that is characterized by a descending order of noise levels: $\sigma_0 = \sigma_{\text{max}} > \sigma_1 > \dots > \sigma_N = 0$. Each noise level corresponds to a specific distribution of the form $\mathbf{x}_i \sim p_{\text{data}}(\mathbf{x}_i; \sigma_i)$. The terminal image of the backward process, \mathbf{x}_N , is expected to approach the original data distribution.

SDE formulation. To present the forward and backward processes rigorously, they can be captured via stochastic differential equations (SDEs). Such SDEs ensure that the sample, \mathbf{x} , aligns with the designated data distribution, p , over its progression through time [48, 22]. A numerical SDE solver can be used here, where a critical component is the noise schedule, $\sigma(t)$, which prescribes the noise level at a specific time, t . A typical noise scheduler is $\sigma(t) \propto \sqrt{t}$. Based on [22], the forward SDE is given as

$$d\mathbf{x} = \sqrt{2\dot{\sigma}(t)\sigma(t)}d\boldsymbol{\omega}(t) \quad (2)$$

while the backward SDE is

$$d\mathbf{x} = -2\dot{\sigma}(t)\sigma(t)\nabla_{\mathbf{x}} \log p(\mathbf{x}; \sigma(t))dt + \sqrt{2\dot{\sigma}(t)\sigma(t)}d\bar{\boldsymbol{\omega}}(t) \quad (3)$$

The term $\dot{\sigma}(t)$ refers to the derivative of $\sigma(t)$. The equations comprises two terms: (i) a deterministic component representing the probability flow ODE and noise degradation; (ii) noise injection via Wiener process. Note that the forward and backward SDE are derived based on the noise schedule $\beta(t) = \dot{\sigma}(t)/\sigma(t)$ that plays a pivotal role by dictating the refresh rate of the noise [48].

Denoising score matching. An examination of the SDE in Eq. (3) indicates the necessity of the score function, $\nabla_{\mathbf{x}} \log p(\mathbf{x}; \sigma)$, for sampling from diffusion models. Intriguingly, this score function remains unaffected by the normalization constant of the base distribution, regardless of its computational complexity. Given its independence, it can be deduced using a denoising method. If $\nabla_{\mathbf{x}} \log p(\mathbf{x}; \sigma) = (D_{\theta}(\mathbf{x}; \sigma) - \mathbf{x})/\sigma^2$, a neural network can be trained for the denoising task using

$$\min_{\theta} \mathbb{E}_{\mathbf{x} \sim p_{\text{data}}} \mathbb{E}_{\mathbf{n} \sim \mathcal{N}(0, \sigma^2 \mathbf{I})} \|D_{\theta}(\mathbf{x} + \mathbf{n}; \sigma) - \mathbf{x}\|^2 \quad (4)$$

5.2 Proposed approach

As discussed in section 2, the high resolution state \mathbf{x} in (1) can be decomposed into the mean $\boldsymbol{\mu}$ and the residual \mathbf{r} . The residual \mathbf{r} will be nearly zero mean and exhibits a small distribution shift, which facilitates

training diffusion models. It is worth noting that this two-stage method has further implications for learning physics. The UNet-regression stage can anticipate many of the physics of downscaling, some of which are deterministic. These include high-resolution topography (which to first order controls the 2-meter temperature variation due to the lapse-rate effect), and the large-scale horizontal wind which combine leading balances in the free atmosphere with the effect of surface friction and topography. Stochastic phenomena such as convective storms that also change temperatures and winds are easier to model as deviations from the mean. Also, cloud resolving models are explicitly formulated using deviations from a larger scale balanced state [35]. In the next section, we discuss the regression and generation stage in details.

5.2.1 Regression on the mean

In order to predict the conditional mean $\boldsymbol{\mu} = \mathbb{E}[\mathbf{x}|\mathbf{y}]$, we resort to UNet-regression. A UNet network is supervised with training data $\{(\mathbf{x}_n, \mathbf{y}_n)\}_{n=1}^N$ to learn the regression. We adopt a UNet architecture that is commonly used in denoising diffusion models. This particular UNet incorporates attention layers and residual layers, allowing it to effectively capture both short and long-range dependencies in the data (see Fig. 1). Mean-Squared-Error (MSE) loss is optimized for training.

5.2.2 Denoising diffusion on the residuals

Once equipped with the UNet-regression network, we can begin by predicting the conditional mean $\hat{\boldsymbol{\mu}}$, which serves as an approximation of $\mathbb{E}[\mathbf{x}|\mathbf{y}]$. Subsequently, we proceed to train the diffusion model directly on the residual component $\mathbf{r} = \mathbf{x} - \hat{\boldsymbol{\mu}}$. Notably, the residual exhibits a small departure from the target data, allowing for the utilization of smaller noise levels during the training of the diffusion process.

In our approach, we adopt the Elucidated diffusion model (EDM), a continuous-time diffusion model that adheres to the principles of SDEs (in Eq. (2)-(3)) [22] to design the diffusion process and architecture. As a result it has an intuitive and physics driven hyperparameter tuning, which makes it work across different domains. In our case, we want to generate the residual \mathbf{r} by sampling from the conditional distribution $p(\mathbf{r}|\mathbf{y})$ following the SDEs in Eq. (2)-(3). To condition the diffusion model, we concatenate the input coarse-resolution data \mathbf{y} with the noise over different channels. We also learn the score function $\nabla_{\mathbf{r}} \log p(\mathbf{r}|\mathbf{y})$ using the score matching loss in Eq. (4) where the denoiser is now $D_{\theta}(\mathbf{r} + \mathbf{n}; \sigma; \mathbf{y})$ with the conditioning input \mathbf{y} . For the denoiser we again follow the desing principles in EDM to use a UNet architecture with skip connections weighted by the noise variance. Architecture details are discussed in Section 5.3.2.

To generate samples from the distribution $p(\mathbf{r}|\mathbf{y})$, we employ the second-order EDM stochastic sampler [22] [Algorithm 2] to solve for the reverse SDE in Eq. (3). Upon sampling the residual \mathbf{r} , we augment it with the predicted conditional mean $\hat{\boldsymbol{\mu}}$ from regresion, to generate the sample $\hat{\boldsymbol{\mu}} + \mathbf{r}$. This entire workflow is illustrated in Fig. 1, providing a visual representation of the steps involved in our proposed method.

5.3 Experimental setup

5.3.1 Dataset

The dataset used in this study is a subset of the proprietary RWRF model data (Radar Data Assimilation with WRFDA ¹). The RWRF model is one of the operational regional Numerical Weather Prediction (NWP) models developed by CWA, which focuses on radar Data Assimilation (DA) in the vicinity of Taiwan. Assimilating radar data is a common strategy used in regional weather prediction, which helps constrain especially stochastic convective processes such as mesoscale convective systems and short-lived thunderstorms.

By incorporating radar data, RWRF improves the short-term prediction of high-impact weather events. The radar observations possess high spatial resolution of approximately 1km and temporal resolutions of 5-10 minutes at a convective scale. These observations provide wind information (radial velocity) as well as hydrometers (radar reflectivity) usefully, with a particular emphasis on the lower atmosphere. The radar data assimilation relies on the availability of reliable and precise observations, which contributes significantly to enhance the accuracy and performance of the applied deep learning algorithms in the context of NWP applications.

¹<https://www.mmm.ucar.edu/models/wrfda>

The dataset covers a duration of 52 months, specifically from January 2018 to April 2022. It has a temporal frequency of one hour and a spatial resolution of 2km. The dataset is represented by a grid of 450x450 points, projected using the Lambert conformal conical projection method around Taiwan. The geographical extent of the dataset spans from approximately 116.371°E to 125.568°E in longitude and 19.5483°N to 27.8446°N in latitude.

Initially, the data is provided in the NetCDF format, which is the output of the WRFDA assimilation process. Subsequently, vertical interpolated from sigma levels to isobaric levels then save as a custom CWA DMS format. As part of the preprocessing steps, the data is converted to the Hadoop Distributed File System (HDFS) format. The preprocessing also includes selecting 20 fields (weather variables at specific height or pressure) as deep learning channels based on the advice of domain experts. Additionally, any missing or corrupted data points represented by "inf" or "nan" values are eliminated from the dataset. This leads to a reduction in the number of samples from 37,944 to 33,813.

Each sample in the dataset consists of 20 channels of information. This includes four pressure levels (500 hPa, 700 hPa, 850 hPa, and 925 hPa) with four corresponding fields: temperature, eastward and northward components horizontal wind vector, and Geopotential Height. Additionally, the dataset includes surface fields such as 2 meter Temperature, 10 meter wind vector, and radar reflectivity.

5.3.2 Network architecture and training

The input data from ERA5 consists of 20 channels at a resolution of 36×36 , while the output data from WRF-CWA consists of 4 channels at a higher resolution of 448×448 . The output channels include radar reflectivity, eastward and northward 10 meter wind vectors, and 2 meter temperature. Notably, the radar reflectivity channel is not present in the input data and needs to be predicted based on the other channels. Thus, while the prediction of wind and temperature could be viewed as a super-resolution task, the prediction of radar is strictly generative. The radar reflectivity data also exhibits a distinct distribution compared to the other output channels, with positive values and a prominent zero-mode consistent with typical non-raining conditions. To facilitate training, we interpolate the global input data onto the curvirectangular grid of CWA with bilinear interpolation. Additionally, we introduce 4 channels for sinusoidal positional embedding. To avoid over-fitting we divide the data into training and testing sets. Four years of data 2018-2020 are used for training (2,4154 samples total). For testing we use the full year 2021 as well as the first four months (January to April) of 2022.

To ensure compatibility and consistency, we employ the same UNet architecture used in EDM (Elucidated Diffusion Models) for both the regression and residual diffusion networks. This architecture is based on the UNet model proposed in [47]. We enhance the UNet by increasing its size to include 6 encoder layers and 6 decoder layers. The base embedding size is set to 128, and it is multiplied over channels according to the pattern [1,2,2,2,2]. The attention resolution is defined as 28. For time embedding in the diffusion process, we utilize Fourier-based position embedding. However, in the regression network, time embedding is disabled. No data augmentation techniques are employed during training. Overall, the UNet architecture comprises 80 million parameters.

During the training phase, we use the Adam optimizer with a learning rate of $2e-4$, $\beta_1 = 0.9$, and $\beta_2 = 0.99$. Exponential moving averages (EMA) with a rate of $\eta = 0.5$ are applied, and dropout with a rate of 0.13 is utilized. The regression network solely receives the input conditioning channels. On the other hand, the diffusion training incorporates the 20 input conditioning channels from the coarse-resolution ERA5 data, which are concatenated with 4 noise channels to generate the output for each denoiser. For diffusion training, we adopt the Elucidated Diffusion Model (EDM), a continuous-time diffusion model. During training, EDM randomly selects the noise variance such that $\ln(\sigma(t)) \sim \mathcal{N}(0, 1.2^2)$ and aims to denoise the samples per mini-batch. EDM is trained for 100 million steps, while the regression network is trained for 30 million steps. The training process is distributed across 16 DGX nodes, each equipped with 8 A100 GPUs, utilizing data parallelism and a total batch size of 512. The total training time for regression and diffusion models was 7 days that amounts to approximately 28, 224 GPU-hours.

For sampling purposes, we employ the second-order stochastic sampler provided by EDM. This sampler performs 18 steps, starting from a maximum noise variance of $\sigma_{\max} = 800$ and gradually decreasing it to a minimum noise variance of $\sigma_{\min} = 0.002$. We adopt the rest of hyperparamaters from EDM as listed in [22].

5.4 Evaluation criterion

Probabilistic predictions aim to maximize sharpness subject to calibration [37]. Qualitatively, calibration means that the likelihood of observing the true value is the same as observing a member drawn from the ensemble. A necessary condition for calibration is that the spread-error relationship be 1-to-1 when averaged over sufficient samples [12]. Calibration also manifests as a flat rank-histogram. A simple metric used below is the root-mean-squared error of the sample mean. In the large sample limit, the sample mean becomes deterministic. So we expect this error to be comparable for generative and deterministic models.

Instead of considering both calibration and spread separately, it can be easier to use proper scoring rules like the continuous-ranked-probability score (CRPS) [14]. Let x be a scalar observation and F be the cumulative distribution of the probabilistic forecast (e.g., the empirical CDF of generated samples). Then, CRPS is defined as

$$CRPS(F, x) = \int_{-\infty}^{\infty} (F(y) - \mathbb{1}_{\{y \geq x\}})^2 dy.$$

The F which minimizes CRPS is the true cumulative distribution of x . For a deterministic forecast, $F(y) = \mathbb{1}_{\{y >= x_0\}}$ where x_0 is the forecast value, CRPS is equivalent to the mean absolute deviation.

6 Acknowledgements

We extend our profound appreciation to the Central Weather Administration (CWA) of Taiwan², a premier government meteorological research and forecasting institution, for granting us access to the invaluable operational Numerical Weather Prediction (NWP) model dataset and for their expert guidance on data consultation. Our gratitude also extends to the AI-Algo team at NVIDIA, especially Kamyar Azizzadenesheli, Anima Anandkumar, Nikola Kovachki, Jean Kossaifi, and Boris Bonev for their insightful discussions. Additionally, we are indebted to David Matthew Hall for his constructive feedback on the manuscript.

References

- [1] Henry Addison, Elizabeth Kendon, Suman Ravuri, Laurence Aitchison, and Peter AG Watson. Machine learning emulation of a local-scale uk climate model. *arXiv preprint arXiv:2211.16116*, 2022.
- [2] Jorge Baño-Medina, Rodrigo Manzananas, and José Manuel Gutiérrez. Configuration and intercomparison of deep learning neural models for statistical downscaling. *Geoscientific Model Development*, 13(4):2109–2124, 2020.
- [3] Monika Barcikowska, Frauke Feser, and Hans Von Storch. Usability of best track data in climate statistics in the western north pacific. *Monthly Weather Review*, 140(9):2818–2830, 2012.
- [4] G. Batzolis, J. Stanczuk, C.-B. Schönlieb, and C. Etmann. Conditional image generation with score-based diffusion models. *arXiv preprint arXiv:2111.13606*, 2021.
- [5] Zied Ben-Bouallegue, Mariana C A Clare, Linus Magnusson, Estibaliz Gascon, Michael Maier-Gerber, Martin Janousek, Mark Rodwell, Florian Pinault, Jesper S Dramsch, Simon T K Lang, Baudouin Raoult, Florence Rabier, Matthieu Chevallier, Irina Sandu, Peter Dueben, Matthew Chantry, and Florian Pappenberger. The rise of data-driven weather forecasting, 2023.
- [6] Kaifeng Bi, Lingxi Xie, Hengheng Zhang, Xin Chen, Xiaotao Gu, and Qi Tian. Accurate medium-range global weather forecasting with 3d neural networks. *Nature*, pages 1–6, 2023.
- [7] Gu-Feng Bian, Gao-Zhen Nie, and Xin Qiu. How well is outer tropical cyclone size represented in the era5 reanalysis dataset? *Atmospheric Research*, 249:105339, 2021.
- [8] Joseph K Blitzstein and Jessica Hwang. *Introduction to probability*. Crc Press, 2019.

²<https://www.cwa.gov.tw/eng/>

- [9] Boris Bonev, Thorsten Kurth, Christian Hundt, Jaideep Pathak, Maximilian Baust, Karthik Kashinath, and Anima Anandkumar. Spherical fourier neural operators: Learning stable dynamics on the sphere. *arXiv preprint arXiv:2306.03838*, 2023.
- [10] Florinel-Alin Croitoru, Vlad Hondru, Radu Tudor Ionescu, and Mubarak Shah. Diffusion models in vision: A survey. *IEEE Transactions on Pattern Analysis and Machine Intelligence*, 2023.
- [11] P. Dhariwal and A. Nichol. Diffusion models beat gans on image synthesis. In *Proceedings of NeurIPS*, volume 34, pages 8780–8794, 2021.
- [12] V Fortin, M Abaza, F Anctil, and R Turcotte. Why should ensemble spread match the RMSE of the ensemble mean? *J. Hydrometeorol.*, 15(4):1708–1713, August 2014.
- [13] Andrew Geiss and Joseph C Hardin. Radar super resolution using a deep convolutional neural network. *Journal of Atmospheric and Oceanic Technology*, 37(12):2197–2207, 2020.
- [14] Tilmann Gneiting and Adrian E Raftery. Strictly proper scoring rules, prediction, and estimation. *J. Am. Stat. Assoc.*, 102(477):359–378, March 2007.
- [15] Aofan Gong, Ruidong Li, Baoxiang Pan, Haonan Chen, Guangheng Ni, and Mingxuan Chen. Enhancing spatial variability representation of radar nowcasting with generative adversarial networks. *Remote Sensing*, 15(13):3306, 2023.
- [16] William J Gutowski, Paul Aaron Ullrich, Alex Hall, L Ruby Leung, Travis Allen O’Brien, Christina M Patricola, RW Arritt, MS Bukovsky, Katherine V Calvin, Zhe Feng, et al. The ongoing need for high-resolution regional climate models: Process understanding and stakeholder information. *Bulletin of the American Meteorological Society*, 101(5):E664–E683, 2020.
- [17] Lucy Harris, Andrew TT McRae, Matthew Chantry, Peter D Dueben, and Tim N Palmer. A generative deep learning approach to stochastic downscaling of precipitation forecasts. *Journal of Advances in Modeling Earth Systems*, 14(10):e2022MS003120, 2022.
- [18] Yusuke Hatanaka, Yannik Glaser, Geoff Galgon, Giuseppe Torri, and Peter Sadowski. Diffusion models for high-resolution solar forecasts. *arXiv preprint arXiv:2302.00170*, 2023.
- [19] Hans Hersbach, Bill Bell, Paul Berrisford, Shoji Hirahara, András Horányi, Joaquín Muñoz-Sabater, Julien Nicolas, Carole Peubey, Raluca Radu, Dinand Schepers, et al. The era5 global reanalysis. *Quarterly Journal of the Royal Meteorological Society*, 146(730):1999–2049, 2020.
- [20] J. Ho, A. Jain, and P. Abbeel. Denoising diffusion probabilistic models. In *Proceedings of NeurIPS*, volume 33, pages 6840–6851, 2020.
- [21] Cathy Hohenegger, Peter Korn, Leonidas Linardakis, René Redler, Reiner Schnur, Panagiotis Adamidis, Jiawei Bao, Swantje Bastin, Milad Behraves, Martin Bergemann, et al. Icon-sapphire: simulating the components of the earth system and their interactions at kilometer and subkilometer scales. *Geoscientific Model Development*, 16(2):779–811, 2023.
- [22] Tero Karras, Miika Aittala, Timo Aila, and Samuli Laine. Elucidating the design space of diffusion-based generative models. *arXiv preprint arXiv:2206.00364*, 2022.
- [23] Naveen Kodali, Jacob Abernethy, James Hays, and Zsolt Kira. On convergence and stability of gans. *arXiv preprint arXiv:1705.07215*, 2017.
- [24] Remi Lam, Alvaro Sanchez-Gonzalez, Matthew Willson, Peter Wirnsberger, Meire Fortunato, Alexander Pritzel, Suman Ravuri, Timo Ewalds, Ferran Alet, Zach Eaton-Rosen, et al. Graphcast: Learning skillful medium-range global weather forecasting. *arXiv preprint arXiv:2212.12794*, 2022.
- [25] Jussi Leinonen, Ulrich Hamann, Daniele Nerini, Urs Germann, and Gabriele Franch. Latent diffusion models for generative precipitation nowcasting with accurate uncertainty quantification. *arXiv preprint arXiv:2304.12891*, 2023.

- [26] Jussi Leinonen, Daniele Nerini, and Alexis Berne. Stochastic super-resolution for downscaling time-evolving atmospheric fields with a generative adversarial network. *IEEE Transactions on Geoscience and Remote Sensing*, 59(9):7211–7223, 2020.
- [27] Lizao Li, Rob Carver, Ignacio Lopez-Gomez, Fei Sha, and John Anderson. Seeds: Emulation of weather forecast ensembles with diffusion models. *arXiv preprint arXiv:2306.14066*, 2023.
- [28] Chenlin Meng, Robin Rombach, Ruiqi Gao, Diederik Kingma, Stefano Ermon, Jonathan Ho, and Tim Salimans. On distillation of guided diffusion models. In *Proceedings of the IEEE/CVF Conference on Computer Vision and Pattern Recognition*, pages 14297–14306, 2023.
- [29] Bin Mu, Bo Qin, Shijin Yuan, and Xiaoyun Qin. A climate downscaling deep learning model considering the multiscale spatial correlations and chaos of meteorological events. *Mathematical Problems in Engineering*, 2020:1–17, 2020.
- [30] National Centers for Environmental Prediction, National Weather Service, NOAA, U.S. Department of Commerce. Ncep gfs 0.25 degree global forecast grids historical archive, 2015.
- [31] Nidhi Nishant, Sanaa Hobeichi, Steven C Sherwood, Gab Abramowitz, Yawen Shao, Craig Bishop, and Andy J Pitman. Comparison of a novel machine learning approach with dynamical downscaling for australian precipitation. *Environmental Research Letters*, 2023.
- [32] Jaideep Pathak, Shashank Subramanian, Peter Harrington, Sanjeev Raja, Ashesh Chattopadhyay, Morteza Mardani, Thorsten Kurth, David Hall, Zongyi Li, Kamyar Azizzadenesheli, et al. Fourcastnet: A global data-driven high-resolution weather model using adaptive fourier neural operators. *arXiv preprint arXiv:2202.11214*, 2022.
- [33] Stephen B Pope. *Turbulent flows*. Cambridge university press, 2000.
- [34] Jordan G Powers, Joseph B Klemp, William C Skamarock, Christopher A Davis, Jimy Dudhia, David O Gill, Janice L Coen, David J Gochis, Ravan Ahmadov, Steven E Peckham, et al. The weather research and forecasting model: Overview, system efforts, and future directions. *Bulletin of the American Meteorological Society*, 98(8):1717–1737, 2017.
- [35] Kyle G Pressel, Colleen M Kaul, Tapio Schneider, Zhihong Tan, and Siddhartha Mishra. Large-eddy simulation in an anelastic framework with closed water and entropy balances. *Journal of Advances in Modeling Earth Systems*, 7(3):1425–1456, 2015.
- [36] Ilan Price and Stephan Rasp. Increasing the accuracy and resolution of precipitation forecasts using deep generative models. In *International conference on artificial intelligence and statistics*, pages 10555–10571. PMLR, 2022.
- [37] Adrian E Raftery, Tilmann Gneiting, Fadoua Balabdaoui, and Michael Polakowski. Using bayesian model averaging to calibrate forecast ensembles. *Mon. Weather Rev.*, 133(5):1155–1174, May 2005.
- [38] Neelesh Rampal, Peter B Gibson, Abha Sood, Stephen Stuart, Nicolas C Fauchereau, Chris Brandolino, Ben Noll, and Tristan Meyers. High-resolution downscaling with interpretable deep learning: Rainfall extremes over new zealand. *Weather and Climate Extremes*, 38:100525, 2022.
- [39] Suman Ravuri, Karel Lenc, Matthew Willson, Dmitry Kangin, Remi Lam, Piotr Mirowski, Megan Fitzsimons, Maria Athanassiadou, Sheleem Kashem, Sam Madge, et al. Skilful precipitation nowcasting using deep generative models of radar. *Nature*, 597(7878):672–677, 2021.
- [40] Eduardo R. Rodrigues, Igor Oliveira, Renato L. F. Cunha, and Marco A. S. Netto. Deepdownscale: a deep learning strategy for high-resolution weather forecast. *arXiv preprint arXiv:1808.05264*, 2018.
- [41] Ashish Routray, Devajyoti Dutta, John P George, and VS Prasad. High resolution rapid refresh data assimilation system at ncmrwf (india) for convection permitting models. *Name of the Journal*, XX(YY):ZZ–ZZZ, 20XX.

- [42] Tim Salimans, Ian Goodfellow, Wojciech Zaremba, Vicki Cheung, Alec Radford, and Xi Chen. Improved techniques for training gans. *Advances in neural information processing systems*, 29, 2016.
- [43] Tim Salimans and Jonathan Ho. Progressive distillation for fast sampling of diffusion models. In *International Conference on Learning Representations*, 2021.
- [44] Badr-eddine Sebbar, Saïd Khabba, Olivier Merlin, Vincent Simonneaux, Chouaib El Hachimi, Mohamed Hakim Kharrou, and Abdelghani Chehbouni. Machine-learning-based downscaling of hourly era5-land air temperature over mountainous regions. *Atmosphere*, 14(4):610, 2023.
- [45] Tobias Selz and George C Craig. Upscale error growth in a high-resolution simulation of a summertime weather event over europe. *Monthly Weather Review*, 143(3):813–827, 2015.
- [46] Jiefeng Song, Chaoyue Meng, and Stefano Ermon. Denoising diffusion implicit models. In *Proceedings of the International Conference on Learning Representations (ICLR)*, 2021.
- [47] Yang Song and Stefano Ermon. Generative modeling by estimating gradients of the data distribution. In *Advances in Neural Information Processing Systems (NeurIPS)*, 2019.
- [48] Yang Song, Jascha Sohl-Dickstein, Diederik P. Kingma, Ashish Kumar, Stefano Ermon, and Ben Poole. Score-based generative modeling through stochastic differential equations. In *Proceedings of the International Conference on Learning Representations (ICLR)*, 2021.
- [49] Bjorn Stevens, Masaki Satoh, Ludovic Auger, Joachim Biercamp, Christopher S Bretherton, Xi Chen, Peter Düben, Falko Judt, Marat Khairoutdinov, Daniel Klocke, et al. Dyamond: the dynamics of the atmospheric general circulation modeled on non-hydrostatic domains. *Progress in Earth and Planetary Science*, 6(1):1–17, 2019.
- [50] B Teufel, F Carmo, L Sushama, L Sun, MN Khaliq, S Bélair, A Shamseldin, D Nagesh Kumar, and J Vaze. Physics-informed deep learning framework to model intense precipitation events at super resolution. *Geoscience Letters*, 10(1):19, 2023.
- [51] Arash Vahdat, Karsten Kreis, and Jan Kautz. Score-based generative modeling in latent space. *Advances in Neural Information Processing Systems*, 34:11287–11302, 2021.
- [52] Emily Vosper, Peter Watson, Lucy Harris, Andrew McRae, Raul Santos-Rodriguez, Laurence Aitchison, and Dann Mitchell. Deep learning for downscaling tropical cyclone rainfall to hazard-relevant spatial scales. *Journal of Geophysical Research: Atmospheres*, page e2022JD038163, 2023.
- [53] Robert L Wilby, TML Wigley, D Conway, PD Jones, BC Hewitson, J Main, and DS Wilks. Statistical downscaling of general circulation model output: A comparison of methods. *Water resources research*, 34(11):2995–3008, 1998.
- [54] Zhisheng Xiao, Karsten Kreis, and Arash Vahdat. Tackling the generative learning trilemma with denoising diffusion GANs. In *International Conference on Learning Representations (ICLR)*, 2022.
- [55] Hongkai Zheng, Weili Nie, Arash Vahdat, Kamyar Azizzadenesheli, and Anima Anandkumar. Fast sampling of diffusion models via operator learning. In *International Conference on Machine Learning*, pages 42390–42402. PMLR, 2023.

Citation	Architecture	Resolutions	Pixels	Variables
Addison et al., (2022) [1]	Diffusion	input: 60km target: 8.8km	64 ²	precipitation
Harris et al., (2022) [17]	GANs + ensemble forecast	input: 10km target: 1km	940 ²	precipitation
Hatanaka et al., (2023) [18]	Cascaded diffusion	input: 30km target: 1km	128 ²	day-ahead solar-irradiance
Leinonen et al., (2020) [26]	GANs	input 8km target: 1km	128 ²	precipitation
Leinonen et al., (2020) [26]	GANs	input 16km target: 2km	128 ²	cloud optical-thickness
Price and Rasp, (2022) [36]	Corrector GAN	input 32km target 4km	128 ²	precipitation
Vosper et al., (2023) [52]	WGAN	input 100km target 10km	100 ²	precipitation from tropical-cyclones
Current work	ResDiff	input 25km target 2km	448 ²	10 meter winds 2 meter temperature radar-reflectivity

Table 2: Downscaling models presented in the most relevant works we could find with respect to the current study. We highlight the resolution ratios, the pixel size of the high resolution prediction, predicted variables and architecture.

7 Supplementary information

7.1 Our position with respect to existing works

To highlight the novel component of our work we expend our review. Table 2 above present a shortlist of the most relevant works that perform weather downscaling. Some of the successes of previous downscaling works are by performing state vector inflation as [1], on a relatively larger domain [17], with a large resolution ratio, e.g. [18, 1] and downscaling precipitation from tropical cyclones [52]. However, most of these related works focus on a single variables per model (note that [26] provided two model each per variable). The variables of interest in all these works are related to properties of cloud and precipitation. While [52] showed a successful super resolution (recovering 10km from data coarsened to 100km) of tropical cyclone precipitation. To the best of our knowledge ML downscaling of tropical cyclones, which requires accounting for different physics, across many channels and channel synthesis was not shown before.

The combined prediction of selected dynamical, thermodynamical and microphysical (cloud related) variables in concert marks a new capability of such models. Its utility is demonstrated here by examining coherent structures and how all variables jointly downscaled in a physically consistent manner.

7.2 Comparison of simulated Typhoons with historical records

Although our out-of-sample data is limited to 2021, we can compare ResDiff simulated typhoons in the CWA region with historical records. The Japan Meteorological Agency best track data (JMA tracks) [3] includes the maximum windspeed (intensity) and radius of maximum windspeed (size) of typhoons in west pacific for several decades. During the years 1980 to 2020 for (which we have ERA5 data available) and within the CWA domain, we identified 648 instances of typhoons with intensities of 30 m/s or greater in this time period. Panels (a) and (b) of figure 7 display the storm size and intensity, respectively, revealing the expected

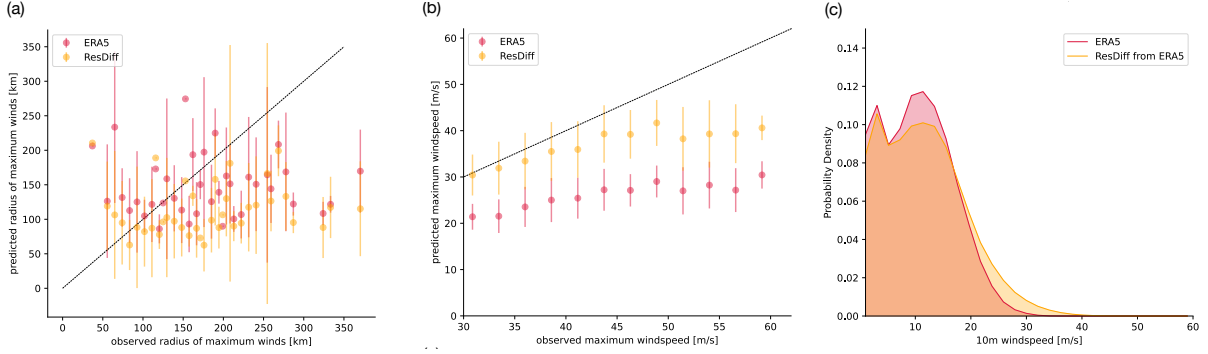


Figure 7: Comparison between ERA5, ResDiff (from ERA5) and observed records for all typhoons found in the domain with windspeed of 30 m/s or more in the years 1980-2020. Panel (a): mean (dot) and one standard deviation (bars) of predicted radius of maximum winds for the ERA5 (red) and ResDiff (orange) storms, grouped by their observed values. These are plotted vs. the observed values. Panel (b) same as (a) but the maximum windspeed. Panel (c): The PDFs of all instances with typhoon of windspeed 30 m/s or greater in the years 1980-2020 in the CWA domain.

correction for ERA5 typhoons achieved through the application of ResDiff. One imperfection of ResDiff is that it shrinks all storms, including those with the correct size or those that were too small in the ERA5 input data (panel a). The main benefit is an improvement in the windspeeds, removing most of the error between the ERA5 and the observed records for windspeeds up to 50 m/s (panel b); stronger storms have room for improvement. ResDiff generates a five-fold increase in the probability of hurricane-force winds exceeding 33 m/s (panel c). To the extent that JMA tracks can serve as ground truth, such distribution shift has significant societal implications as these low-probability, high-impact events represent a substantial portion of the overall risk, underscoring the importance of accurate modeling and forecasting.

7.3 Proof of small variance for residuals

In section 2, it was claimed that using regression step to form the residual term leads to smaller data variance and thus generative learning for distribution matching becomes easier. Here, we prove that is generally true if the regression step gives a good surrogate for the mean, namely $\mu \approx \mathbb{E}[\mathbf{x}|\mathbf{y}]$. Recall that \mathbf{y} and \mathbf{x} are the input and target respectively. Ideally, the residual is formed as $\mathbf{r} = \mathbf{x} - \mathbb{E}[\mathbf{x}|\mathbf{y}]$. Consider one pixel from each and call those random variables X and R respectively. From the Law of Total Variance [8], we can then decompose the variance as follows

$$\text{var}(X) = \mathbb{E}[\text{var}(X|\mathbf{Y})] + \text{var}(\mathbb{E}[X|\mathbf{Y}])$$

From the residual term $R = X - \mathbb{E}[X|\mathbf{Y}]$, one can readily deduce that

$$\mathbb{E}[R|\mathbf{Y}] = 0, \quad \text{var}(R|\mathbf{Y}) = \text{var}(X|\mathbf{Y})$$

As a result,

$$\begin{aligned} \text{var}(R) &= \mathbb{E}[\underbrace{\text{var}(R|\mathbf{Y})}_{=\text{var}(X|\mathbf{Y})}] + \text{var}(\underbrace{\mathbb{E}[R|\mathbf{Y}]}_{=0}) \\ &\leq \mathbb{E}[\text{var}(X|\mathbf{Y})] + \underbrace{\text{var}(\mathbb{E}[X|\mathbf{Y}])}_{\geq 0} = \text{var}(X) \end{aligned}$$

The gap is due to $\text{var}(\mathbb{E}[X|\mathbf{Y}])$ which is significant when the mean has large variations. Note that here we analyze the variance of a single pixel since the forward process also perturbs each pixel independently.